Transient Nascent Adhesion at the Initial Stage of Cell Adhesion Visualized on a Plasmonic Metasurface

Lee, Shi Ting
Institute for Materials Chemistry and Engineering Kyushu University

Kuboki, Thasaneeya
Institute for Materials Chemistry and Engineering Kyushu University

Kidoaki, Satoru
Institute for Materials Chemistry and Engineering Kyushu University

Aida, Yukiko
Institute for Materials Chemistry and Engineering Kyushu University

他

https://hdl.handle.net/2324/7181970

Transient Nascent Adhesion at the Initial Stage of Cell Adhesion Visualized on a Plasmonic Metasurface

Shi Ting Lee, Thasaneeya Kuboki, Satoru Kidoaki, Yukiko Aida, Sou Ryuzaki, Koichi Okamoto, Yusuke Arima,* and Kaoru Tamada*

A plasmonic metasurface composed of self-assembled gold nanoparticles enables high-speed interfacial imaging with high axial and lateral resolution down to the theoretical limit under a widefield microscope. This high-spatiotemporal resolution imaging method monitors "early molecular events" in the adhesion of 3T3 fibroblasts expressing Venus-paxillin and LifeAct-mScarlet, revealing unique transient cell dynamics. Upon attaching to the SiO_2-coated plasmonic metasurface, cells exhibit fibrous nascent adhesions spreading radially at the periphery, together with actively moving membrane blebs. These fibrous nascent structures exist transiently during passive spreading and disappear upon transition to active spreading with mature focal adhesions (FAs). The structure forms on a poor-cell-adhesive SiO_2-coated surface but not on a fibronectin-preadsorbed cell-adhesive surface, suggesting that it temporarily anchors cells to the interface but maintains freedom before active cell spreading. These momentary molecular-level phenomena at the nanointerface are successfully captured by the herein described high-spatiotemporal resolution live-cell imaging method using a plasmonic metasurface.

1. Introduction

Cells respond to the environment and/or external chemical and physical stimuli, leading to proliferation and differentiation.[1–9]

S. T. Lee, T. Kuboki, S. Kidoaki, Y. Aida, S. Ryuzaki, Y. Arima, K. Tamada
Institute for Materials Chemistry and Engineering
Kyushu University
Fukuoka 819-0395, Japan
E-mail: arima@ms.ifoc.kyushu-u.ac.jp; tamada@ms.ifoc.kyushu-u.ac.jp

K. Okamoto
Department of Physics and Electronics
Osaka Prefecture University
Osaka 599-8531, Japan

K. Tamada
Advanced Institute for Materials Research (AIMR)
Tohoku University
Sendai 980-8577, Japan

The ORCID identification number(s) for the author(s) of this article can be found under https://doi.org/10.1002/anbr.202100100.

The adhesion of cells to substrates is the initial step in determining cellular responses against biomaterials. Cell adhesion is known to depend on the surface properties of substrates and the preadsorption of extracellular matrix (ECM) proteins on the substrates.[2,3,9,10] Cells that adhere to substrates start spreading (deforming to a flattened shape) by forming focal adhesions (FAs) that consist of multiprotein assemblies at the adhesion interface.[7,11–13] FAs anchor cells to the substrate via the interaction between the integrin molecule of the cell membrane and the ECM, tension is generated in the actin filaments that form the cytoskeleton, and the cells stretch and proliferate.[7,10,14] When cells spread on sufficiently stiff substrates, bundles of actin filaments, called "stress fibers (SFs)," form and associate with FAs or further aggregate FAs and contribute to cell migration.[7] FAs are also known as "mechanosensors" of the adhered substrate, as they are the site of force transmission of stress generated within the cytoskeleton and the ECM.[10,15,16] FAs contribute to the differentiation of stem cells and are recognized as a research target in mechanobiology.[6,17,18]

Over the years, FAs have been the main target of microscopic studies of adhered cells because of their suitability for conventional microscope imaging in terms of both spatial and temporal resolution.[8,16] The size of mature FAs is typically $1-5\,\mu m$, and the speed of cell migration is approximately $0.1\,\mu m\,min^{-1}$, which is exactly appropriate for the conventional time-lapse imaging method with confocal laser scanning microscopy (CLSM) or total internal reflection fluorescence (TIRF) microscopy.[8,19–23] In such studies, the number of FAs is often counted to assess the cell affinity for the substrate.[7,16] As the latest achievement, the development of super-resolution microscopy enabled the visualization of "nascent" FAs (typically 250 nm in size), which are dot-like transient adhesions with a relatively short lifetime.[8] Nascent adhesion is composed of integrins, actin linkage molecules (talin and vinculin), and signaling molecules, similar to mature FAs.[7,8] However, unlike mature FAs, nascent FAs have not been well characterized, especially in terms of their dynamics, because of the difficulty of achieving both super-resolution and high-speed imaging.[24] Super-resolution localization microscopy, such as stochastic optical reconstruction microscopy (STORM) and photoactivated localization microscopy (PALM),

provides nanospatial resolution images, but the temporal resolution is quite low and cannot monitor millisecond- to second-scale molecular dynamics.[25–28] Therefore, imaging with these techniques is still limited to large FAs in well-adhered cells on substrates with preadsorbed ECM proteins because nascent adhesion structures are expected to have short lifetimes. It is also difficult to sustain fine adhesion structures of weakly adhered cells after fixation. The most popular and effective commercial equipment for high-resolution and high-speed imaging at present is likely confocal spinning-disk microscopy, which provides a lateral resolution of 200 nm and an axial resolution of 800 nm (with a piezo z-stage, it can be reduced to 350 nm) for high-numerical aperture (NA) objectives.[29–31] The disk rotation speed is fast enough (e.g., 10 000 rpm, 10 scans in 5 ms) that it does not affect the frame speed. The exposure times required for high-resolution imaging of live cells determine the temporal resolution, which is typically 0.1−1 s at 100% laser power with a conventional CCD camera when photobleaching caused by the high-power laser is not a main concern for an experiment.[31] Therefore, it is still difficult to visualize cell dynamics at the initial stage of cell adhesion on substrates because fixation of weakly adhering cells or imaging the cells with intense excitation light may result in detachment of cells from the substrate or loss of fine nascent adhesion structures. Live-cell imaging with both high spatial and temporal resolutions enables us to observe early cell adhesion dynamics to substrates.

The fluorescence imaging technique that we recently developed and utilized in this study is based on a plasmonic metasurface composed of self-assembled gold nanoparticles (NPs).[32,33] A self-assembled monolayer of homogeneously sized NPs was fabricated at the air−water interface and transferred onto a coverslip. Compared with other super-resolution microscopy techniques, our plasmonic metasurface-mediated imaging technique is extremely simple but highly effective for monitoring fast molecular-level dynamics at a nanointerface. The localized surface plasmon resonance (LSPR) of the plasmonic metasurface provides high-contrast interfacial images due to the light confined within a few tens of nanometers from the particles and the enhancement of fluorescence.[32] That improves lateral resolution reaching to the theoretical limit (a lateral resolution of a few pixels, with one pixel equivalent to 65 nm, as estimated by size of resolved bright spots[33]) and an axial resolution of ≈20 nm (estimated by exponential decay of LSPR field from finite-difference time-domain [FDTD] simulation[32]). The plasmonic metasurface-mediated imaging allows for live-cell imaging with high spatial resolutions even during cell movement due to the properties of the metasurface, which has an extremely high refractive index and acts as a nanothickness plane light emitter.[33] We also found that the plasmonic metasurface minimizes photobleaching owing to the increase in the emission efficiency via plasmon–exciton coupling, which is an important advantage for maintaining high contrast and resolution in long-term live-cell imaging.[33] Previous studies observed matured FAs of well spread cells after overnight incubation in order to establish the methodology for live-cell imaging using our plasmonic metasurface. Taking advantages of our plasmonic metasurface-mediated imaging technique such as high spatial resolution and minimal photobleaching, we apply our imaging technique to observe initial cell adhesion behavior where cells start to adhere through weak and unstable interactions susceptible for photobleaching.

In this study, we focused on "early molecular events" in the adhesion of 3T3 fibroblasts expressing dual-colored fluorescence with Venus-paxillin and LifeAct-mScarlet, where the cell dynamics at molecular level on a SiO₂-coated surface with and without fibronectin preadsorption were carefully monitored. The very early stage of cell adhesion behavior has not been investigated systematically because of the difficulty of monitoring the molecular-level dynamics with sufficient resolution. In this study, we specifically targeted nascent clusters that appeared at the early stage of "passive" spreading, that is, before the transition to the stage of active spreading with mature FAs, and found unique fibrous nascent adhesions spreading radially at the periphery of the attached cells, together with actively moving membrane blebs.
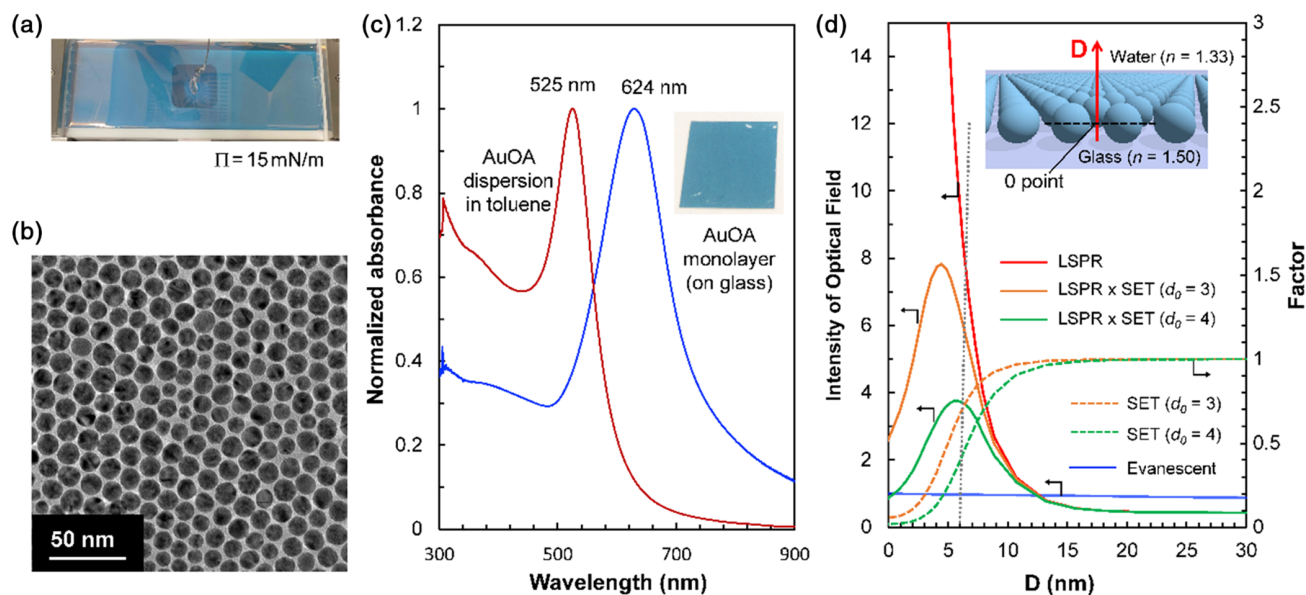
Our aim was to investigate how the cell decides to proceed with attachment, adhesion, and eventually spreading on a material surface by using our high-spatiotemporal resolution interfacial imaging.

2. Results and Discussion

2.1. Principle of High-Resolution Imaging Using a Plasmonic Metasurface

Self-assembled monolayers (SAMs) composed of oleylamine-coated gold nanoparticles (AuOAs) with a diameter of 11.8 ± 1.4 nm were fabricated in a Langmuir−Blodgett (LB) trough.[33] The self-assembly process of AuOAs at the air–water interface, from the evaporation of toluene to solid-like domain formation, is described in Figure S1 and Video S1, Supporting Information. The solid-like domains were gathered together by Teflon bars and compressed until the surface pressure (Π) reached 15 mN m⁻¹ (**Figure 1**a) and then transferred onto a hydrophobized glass coverslip via the Langmuir−Schaefer (LS) method. The AuOA monolayer exhibits a homogeneous, close-packed structure with a gap distance of 1.5 ± 0.4 nm, as determined by the interdigited alkyl chains of oleylamine capping molecules (Figure 1b). The LSPR band excited on the sheet exhibits a large red shift (≈100 nm) from that in solution due to the "collective" excitation of LSPR in the sheet (Figure 1c). In the case of 2D nanosheet, collective excitation of LSPR on the sheet produces homogeneous and strong LSPR field on the entire surface even with local variation in the particle size and the gap distance of a few nm.[34] Furthermore, the particle size and gap distance are significantly smaller than the single pixel size (65×65 nm) of fluorescence image. Therefore, AuOA sheets are considered to be of sufficient quality as substrates for high-resolution imaging through the plasmonic metasurface.

The intensity of the optical field excited on the self-assembled AuOA sheet was calculated using the FDTD method with the periodic boundary model (the red solid line marked as "LSPR" in Figure 1d).[32] The model structure of the AuOA monolayer (the insertion) was made based on the transmission electron microscope (TEM) image, and the intensity of the LSPR field was calculated on line D (the center position of the adjacent particles was set to $D = 0$). The obtained intensity of the LSPR

**ADVANCED
SCIENCE NEWS**

www.advancedsciencenews.com

**ADVANCED
NANOBIOMED
RESEARCH**

www.advnanobiomedres.com

Figure 1. a) A picture of the AuOA monolayer at the air–water interface. b) TEM image of AuOA monolayer. c) LSPR spectrum of AuOAs dispersed in toluene and AuOA monolayers transferred onto a hydrophobized glass slip. d) Comparison of the intensity of the optical field excited by LSPR and TIR. The LSPR field intensity (the red solid line) was calculated by FDTD simulation with the model of the AuOA monolayers under S-polarized light incidence. The evanescent field (the blue solid line) was calculated at the glass/water interface. The orange or green solid lines correspond to "LSPR×SET" with SET distances of $d_0 = 3$ or 4 nm. The fluorescence attenuation factors due to SET are shown by the orange or green dashed lines.

field was 50 times stronger at the maximum point and decayed drastically along the distance of D. In contrast, the decay length of the evanescent wave was significantly longer compared with LSPR, as shown by the solid blue line in Figure 1d ($d = 125$ nm at $\lambda = 561$ nm and $\theta = 65°$).[35] The intensities of the LSPR field and the evanescent field have an intersection at $D = 13$ nm, which indicated that fluorescence enhancement by LSPR could be observed only in the region of $D < 13$ nm in the calculation. We must note that the calculated values of the penetration depths of LSPR should be underestimated in the current FDTD calculation because the periodic boundary model with 3×10 particles as the basic unit could not completely reproduce the effect of the collective excitation of LSPR.[36]

In our previous study, we investigated the influence of S- and P-polarized light incidence on the quality of images on two-dimensionally assembled silver nanoparticles.[37] The FDTD simulation demonstrated that S-polarized light induced strong plasmon coupling at the nanogap between adjacent particles, which led to a highly confined electric field at the nanointerface and provided better image contrast. In contrast, the LSPR field excited by P-polarized light was located on the individual particles, having a relatively long tail in the axial direction and eventually providing slightly stronger total fluorescence.[37] In this study, we utilized S-polarized light for imaging to emphasize contrast over brightness.

In Figure 1d, the orange and green lines marked as "LSPR×SET" are the LSPR field intensities obtained as the products of LSPR and surface energy transfer (SET).[32] The SET is known as an analog of Förster resonance energy transfer (FRET), which demonstrates a d^{-4} dependence. The efficiency of SET depends on the spectrum overlap between the LSPR band and the fluorescence in a similar manner to LSPR-enhanced
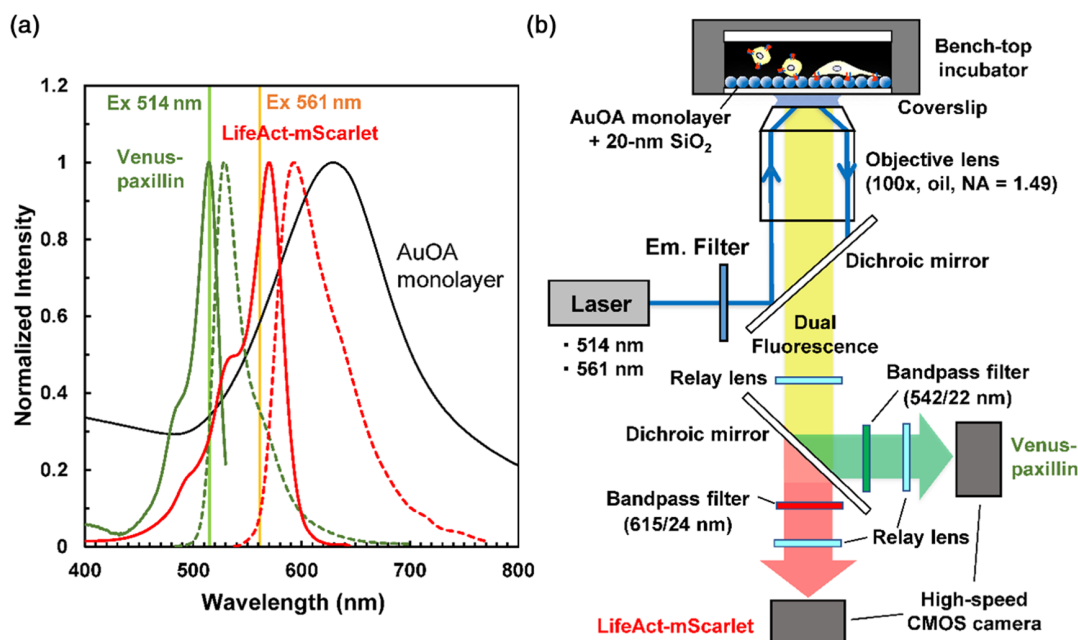
fluorescence, which makes the prediction of the practical "LSPR×SET" value quite difficult.[38] In any case, the penetration depth of the LSPR is not influenced by the SET distance, as shown in Figure 1d, and should be longer than the calculated value but much shorter than the depth of the evanescent field. In fact, we obtained the maximum enhanced fluorescence in the experiments with quantum dots (QDs) or fluorescence beads with a 20 nm SiO_2 spacer layer deposited on the AuOA sheet, i.e., the penetration depth of LSPR should be longer than 20 nm.[32,36] In this study, we used a 20 nm-thick SiO_2 spacer layer on a AuOA sheet to avoid fluorescence quenching and obtained the maximum fluorescence enhancement.[39] For the experiments with a protein-preadsorbed surface, a 10 nm SiO_2 evaporation layer was mainly utilized by taking into account the thickness of the protein layers.

We also should note that an extraordinarily high refractive index and extinction coefficient of the AuOA sheet due to the collective excitation of LSPR ($n = 2.8$ and $k = 2.0$ at 600 nm) improved the lateral resolution down to the theoretical limit. This is not only due to the prediction by Abbe's equation with extraordinarily high refractive index materials but also due to the characteristics of plasmonic metasurfaces, which shorten the exciton lifetime due to surface plasmon (SP)–exciton coupling and reduce the size of local emission points ("nanothickness plane light emitter").[40]

2.2. Imaging of Transient Fibrous Nascent Adhesion on a SiO$_2$-AuOA Surface

In this experiment, fluorescence time-lapse images of live cells were captured using a commercialized TIRF microscope

**ADVANCED
SCIENCE NEWS**

www.advancedsciencenews.com

**ADVANCED
NANOBIOMED
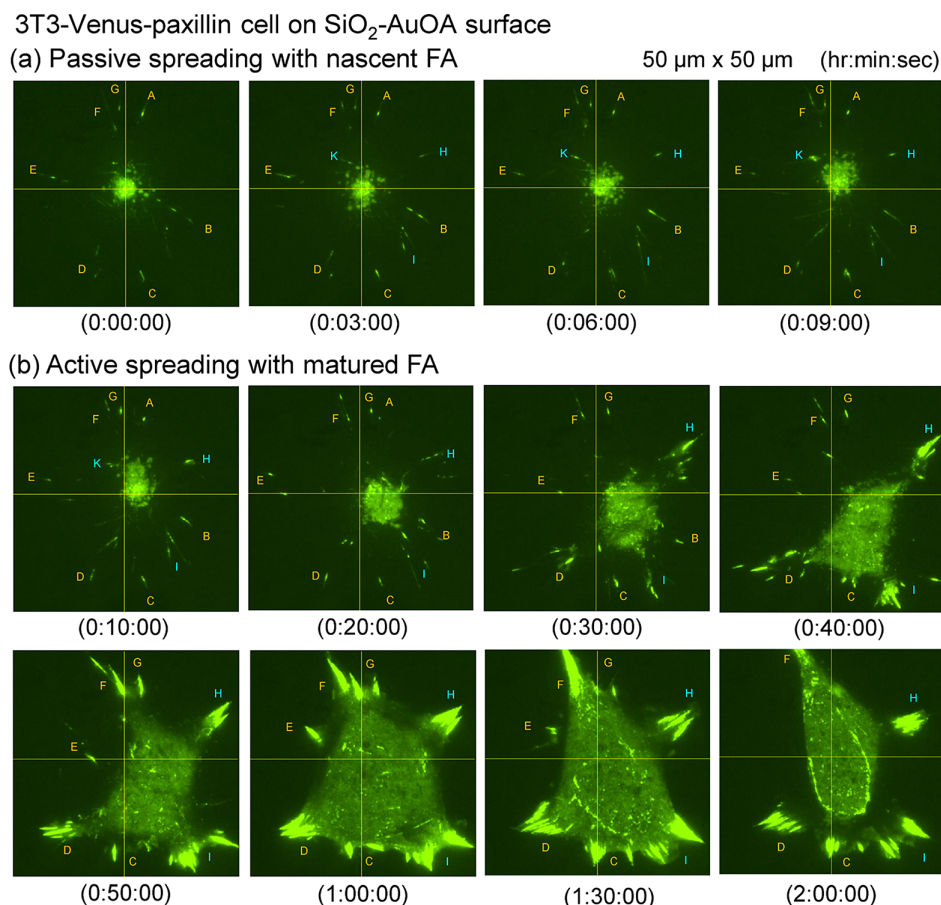RESEARCH**
Open Access

www.advnanobiomedres.com

Figure 2. a) LSPR band of the AuOA monolayer and excitation/emission spectra of Venus-paxillin (Ex 515 nm/Em 528 nm) and LifeAct-mScarlet (Ex 569-nm/Em 594-nm). b) A schematic drawing of TIRF microscopy equipped with a high-speed, dual-color imaging system.

equipped with a multiple-wavelength laser and a dual-camera image-splitting optical system with two sets of high-speed CMOS cameras (**Figure 2**). For dual-color imaging, the sample cell was irradiated simultaneously with both lasers, and fluorescence images of Venus-paxillin and LifeAct-mScarlet were captured simultaneously under the exact same time-lapse condition without time delay. The LSPR band of the AuOA monolayer overlapped the excitation and emission spectra for LifeAct-mScarlet, while only emission spectra for Venus-paxillin, i.e., LSPR-enhanced fluorescence was stronger for LifeAct-mScarlet than for Venus-paxillin. To adjust the two florescence intensities to the same level, we set the excitation laser for Venus-paxillin to twice the power (10 mW) used for LifeAct-mScarlet (5 mW). The excitation lights were blocked by a shutter when the fluorescence images are not captured to avoid photobleaching by continuous illumination.

In this study, we successfully visualized early molecular events that unfolded immediately after the first cell contacted the substrate by following an experimental procedure. First, the focal plane of the microscope was approximately adjusted by using a bright-field image and then switched to fluorescence TIRF mode to allow fluorescent protein-expressing cells to approach the surface. Next, the focal plane was precisely readjusted by using the fluorescence of attached cells at the nanointerface in the field of view, and the view was slightly shifted to the fresh surface to wait for the moment of new cell adhesion. In this procedure, the confined fluorescence only at the nanointerface helped to find the focal plane in a short period of time. The advantage of this plasmonic metasurface-mediated imaging method is high-spatiotemporal resolution.[33] However, it is not rational to start high-speed imaging without knowing the moment of adhesion, so we started time-lapse imaging at reasonable intervals (e.g., 30 s or a few minutes) until a cell adhered.

After cell adhesion, the timing used to capture the images was controlled manually according to the speed of cell dynamics (time intervals varied from no interval to 5 min). Readjusting of focal plane was not necessary during time-lapse observation because our method produces the confined fluorescence only at the nanointerface.

Figure 3 shows selected time-lapse images of a 3T3-Venus-paxillin cell on a SiO2-AuOA surface under a widefield TIRF microscope, where the emission from Venus-paxillin is displayed in "green." Figure 3a shows the moment of the first cell contact and subsequent passive spreading. Immediately after cell contact with the surface, very fine "fibrous nascent adhesions" were observed spreading radially in all directions surrounding the cell contact point (A–G and additional H–K). The formation of this fibrous nascent adhesion took approximately 10−20 min, and the radially spread structure remained stable for ≈10 min thereafter. This radially spreading fibrous structure definitely plays a role in stabilizing early cell adhesion. Careful observation revealed that there were no major changes in the structure and positions of adhesion points (A–G), while the membrane blebs at the cell contact point moved drastically. The original cell contact position is marked by the intersection of the yellow lines. Figure 3b shows the transition from passive spreading to active spreading, where the cell contact position started to shift to the right at 0:10:00 and the position of the adhesion points also moved to the right. Here, the main adhesion of A disappeared, and instead H, D and I grew to become the main adhesions and formed a well-balanced triangular cell morphology at the adhered interface (0:40:00). Ten minutes later (0:50:00), the adhesions in the opposite direction of the triangular cell (F, G) were strengthened, and the cell moved abruptly in that direction (2:00:00). At this stage, a mature FA was formed, while the fibrous nascent adhesions disappeared completely. To show the reproducibility of this
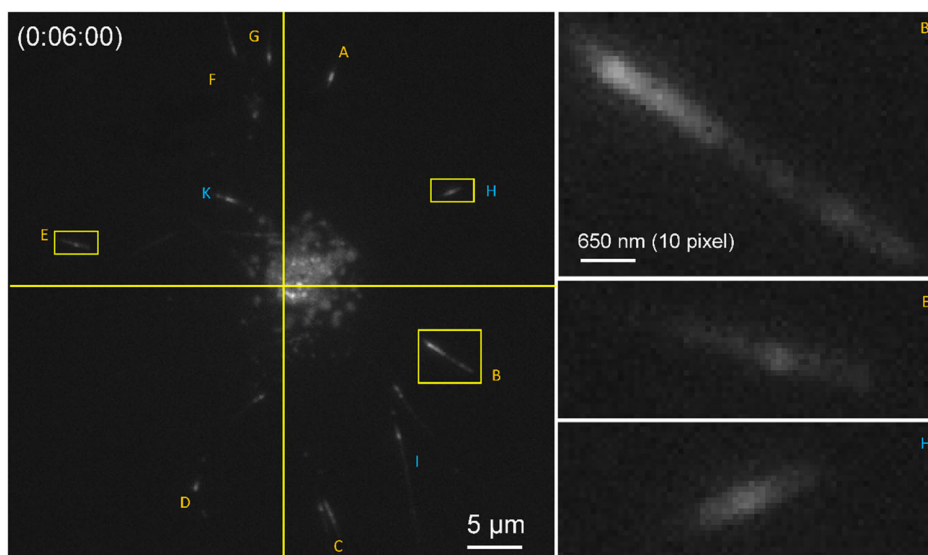
**ADVANCED
SCIENCE NEWS**

www.advancedsciencenews.com

**ADVANCED
NANOBIOMED
RESEARCH**
Open Access

www.advnanobiomedres.com

3T3-Venus-paxillin cell on SiO₂-AuOA surface
(a) Passive spreading with nascent FA   50 μm x 50 μm   (hr:min:sec)

(b) Active spreading with matured FA

Figure 3. Selected time-lapse images of 3T3-Venus-paxillin cells on a SiO₂-AuOA surface under a TIRF microscope (incident angle: 67.5°) with an exposure time of 500 ms. a) Passive spreading with fibrous nascent adhesion. b) Change from passive spreading to active spreading with mature FA. Both the contrast and the brightness are enhanced by 10% by image processing. The video images (Video S2) and the images captured at 1 min intervals (0:00:00 to 1:00:00) and at 5 min intervals (1:00:00 to 2:35:00) are available in the Supporting Information (Figure S2).

phenomenon, another image of the first cell contact is presented in Figure S3 and Video S3, Supporting Information.

Figure 4 shows high-resolution images of fibrous nascent adhesions magnified to pixel resolution (65 nm/pixel) on a SiO₂-AuOA surface. The size of fibrous nascent adhesions is typically 300 nm in width and 1−10 μm in length. Superimposed images composed of bright-field and TIRF images on a SiO₂-AuOA surface (**Figure 5**a and Video S4, Supporting Information) revealed that these thin fibrous nascent adhesions (A–E) can be observed not by bright-field imaging of the cell body but by fluorescence imaging at the nanointerface. Notably, fibrous structures were observed under live-cell monitoring. Some super-resolution microscopies require fixation of cells and capturing multiple images. It is difficult to fix cells at such an early stage of cell adhesion because cells weakly adhere to a substrate and the fibrous structures are very thin. The fixation step might change the morphology of weakly adhered cells and their fine structures. Live-cell imaging was also performed on glass under normal TIRF microscopy conditions. However, it was difficult to obtain the images on glass due to the rapid photobleaching of fibrous nascent adhesion (data not shown). The
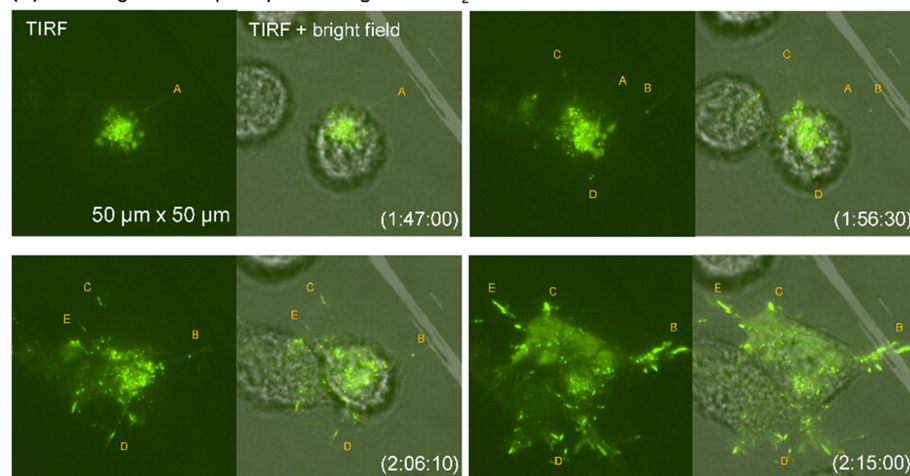
imaging method using a plasmonic metasurface, which allows for live-cell monitoring with high spatial resolution and minimal photobleaching, should be essential to monitor such transient fibrous nascent adhesion at the early stage of cell adhesion to a substrate.

Dual-color images of 3T3 fibroblasts expressing Venus-paxillin and LifeAct-mScarlet were not as clear as single-color images of 3T3-Venus-paxillin cells because of the background emission from LifeAct-mScarlet, which is much stronger than that of Venus-paxillin. This is due to different mechanism of plasmon-enhanced fluorescence between two fluorescent proteins as mentioned in Section 2.2 with Figure 2. Venus-paxillin, for which only emission light is enhanced by plasmon, can have better contrast than LifeAct-mScarlet, for which both excitation and emission lights are enhanced by plasmon. Nevertheless, we confirmed similar long thin fibrous structures appearing green in the image (F and G in Figure 5b), suggesting that they consisted of paxillin proteins. There were red-colored short and thicker fiber-like structures as well, but as they did not extend radially from the cell contact point, they were identified as actin filaments (Figure S4 and Video S5, Supporting Information).
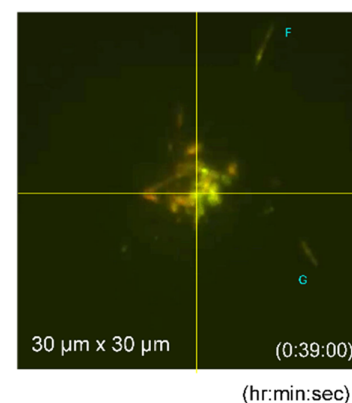
**ADVANCED
SCIENCE NEWS**

www.advancedsciencenews.com

**ADVANCED
NANOBIOMED
RESEARCH**
Open Access

www.advnanobiomedres.com

Figure 4. High-resolution images of "fibrous nascent adhesions" magnified to pixel resolution (65 nm/pixel) on a 20 nm SiO$_2$-AuOA surface. The original image corresponds to the image at (0:06:00) in Figure 3a.

Figure 5. a) Selected time-lapse images of a 3T3-Venus-paxillin cell on a SiO$_2$-AuOA surface; left: TIRF images (incident angle: 67.5°), right: TIRF/bright-field superimposed image. The contrast and brightness are not controlled. The images are captured from Video S4. b) Dual-colored image of a 3T3 cell with Venus-paxillin (green) and LifeAct-mScarlet (red) on a SiO$_2$-AuOA surface (TIRF microscope, incident angle: 75°). The contrast and brightness were enhanced by 20% and 50%, respectively. The images are captured from Video S5. All images were captured with an exposure time of 500 ms.

2.3. Adhesion on a Fibronectin-Preadsorbed SiO$_2$-AuOA Surface

The formation of fibrous nascent adhesions during early-stage cell adhesion is a significant and interesting phenomenon. The role of transient anchoring of the cells to the interface by fibrous nascent adhesions while maintaining a certain degree of freedom during the period before active cell spreading is quite clear. If fibrous nascent adhesion radially spreading to surround the cell contact point (such as the frame thread of a spider web) is formed to prevent cell detachment, this phenomenon should be largely influenced by the substrate. The adhesion of cells to artificial substrates is affected by the surface properties of substrates
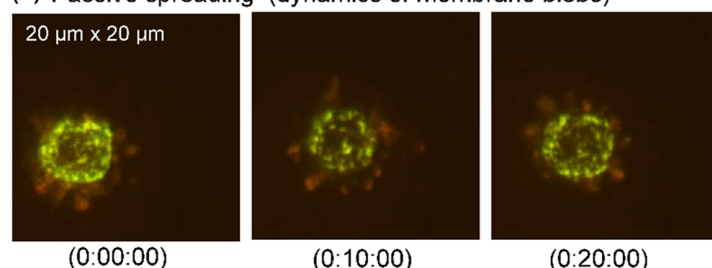
through the nonspecific adsorption of serum proteins in culture medium or by preadsorption of substrates with ECM proteins.[3] To investigate the effect of the substrate on early cell adhesion events, we monitored cell adhesion on a surface with pread-sorbed fibronectin, which is a known cell-adhesive protein in serum.[2]

Dual-colored images taken on the fibronectin-preadsorbed SiO$_2$-AuOA surface with 3T3 fibroblasts expressing both Venus-paxillin and LifeAct-mScarlet are shown in **Figure 6**. Separated images for Venus-paxillin and LifeAct-mScarlet are also available in Figure S5, Supporting Information. As shown in Figure 6a, the effect of preadsorbed fibronectin was obvious
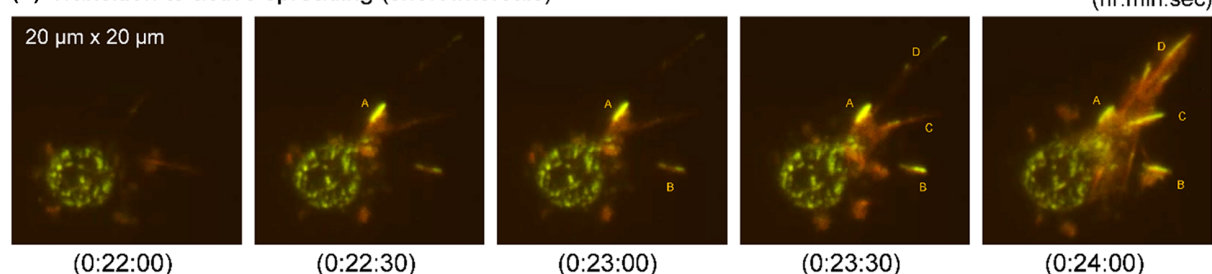
**ADVANCED
SCIENCE NEWS**

www.advancedsciencenews.com

**ADVANCED
NANOBIOMED
RESEARCH**
Open Access

www.advnanobiomedres.com

Figure 6. Selected time-lapse images of dual-colored 3T3 cells with Venus-paxillin (green) and LifeAct-mScarlet (red) on a fibronectin-preadsorbed SiO$_2$-AuOA surface. a) Passive spreading (dynamics of membrane blebs). b) Transition to active spreading. c) Formation of mature FA. The images were taken under a TIRF microscope (incident angle: 75°) with an exposure time of 500-ms. Separated images for Venus-paxillin and LifeAct-mScarlet (Figure S5), the images taken without intervals (Figure S6) and the video image (Video S6) are available in the Supporting Information.

in passive spreading during early-stage cell adhesion, where fibrous nascent adhesions were hardly observed on the surface. In addition, the cluster formation of paxillin proteins (green fluorescence) along the edge of the cell contact region was clearly visualized on the fibronectin-preadsorbed surface, which is in good agreement with a previous report.[2,16] In the case of cell adhesion on the SiO$_2$-AuOA surface, cluster formations aligned on the circumference were not observed. On the other hand, this dual-colored imaging revealed that the membrane blebs actively moving during the early stage of passive spreading mainly contained LifeAct-mScarlet rather than Venus-paxillin or were under the influence of FRET, as shown by their red fluorescence.[41,42]

The spreading of cells on the fibronectin-preadsorbed surface was much faster than that on the SiO$_2$-coated surface, and mature FA formation was completed within 30 min after the first contact of the cell with the surface. Figure 6b,c shows the transition from passive spreading to active spreading and the formation of mature FAs on the fibronectin-preadsorbed surface. As shown, a rapid and drastic morphology change occurred within a short period of time.

The image in Figure 6b reveals that the mature FA marked by A suddenly formed in a similar manner to H (0:40:00) in Figure 3b, together with SFs composed of red-colored actin filaments. Active cell spreading continued in the same direction and led to the growth of other mature FAs (B, C, D). As both of these mature FAs were composed of both Venus-paxillin and LifeAct-mScarlet, they appeared yellow. Interestingly, the original clusters composed of green-colored nascent FAs and red-colored membrane blebs located at the first contact area remained during this active spreading process. Figure 6c displays active spreading to the triangle shape in a similar manner to the image in Figure 3b, where the cell maintained a balance of tension in the directions of D, G, and E. The spreading of the cell in the G and E directions was extremely fast and completed within 10 s. Even during this process, the cell maintained the original round clusters composed of green-colored nascent FAs on the left of the cell body. Independently, the networked structure of the red-colored actin cytoskeleton was confirmed across the cell body. Finally, the cell spread to a round shape with actin filaments and mature FAs at the periphery of the whole cell

body (Figure S7, Supporting Information). Images of 3T3-Venus-paxillin cells with only green fluorescence on the fibronectin-preadsorbed SiO_2-AuOA surface are also available in Figure S8 and Video S7, Supporting Information, where the absence of fibrous nascent adhesions is clearly shown in images with low background noise.

In this study, high-spatiotemporal resolution imaging with a plasmonic metasurface revealed the formation of fibrous nascent adhesions spreading radially to surround the cell contact point. This feature was observed only on surfaces with poor-cell-adhesive SiO_2-AuOA surfaces but not on cell-adhesive fibronectin-preadsorbed surfaces, suggesting that the role of fibrous nascent adhesions is temporary anchoring of the cells to the substrate.

Figure 7 is a schematic drawing of surface-selective early-stage cell adhesion on SiO_2 and fibronectin-coated surfaces. This

fibrous nascent adhesion holds a certain morphological similarity to filopodia, that is, thin ($\approx$200 nm in diameter) tubular protrusions generally formed at the front of lamellipodia that play a sensory role in addition to their direct role in migration, probing substrate properties and driving pathfinding.[43] However, considering the role of this fibrous nascent adhesion, which transiently appears only at the very early stage of cell adhesion and stabilizes the cell contact point by spreading radially like the frame thread of a spider web, it seems appropriate to classify this as a different category of cellular structure.

These transient, molecular-level structures formed at the nanointerface must be very sensitive to the properties of the contact substrate and the ability of cells to adhere to substrates and to respond to various stimuli. We expect this fibrous structure and observation of its dynamics to have potential applications not only in cell adhesion tests of culture substrates but also in single-cell analysis, such as stimulus response or drug sensitivity, cell discrimination between normal cells and cancer cells, and early identification of stem cell differentiation in the field of cell biology.[44–46] In these studies, the high-spatiotemporal resolution live-cell imaging method using plasmonic metasurfaces will be a key technology, taking an additional advantage of plasmonic metasurfaces, which minimize photobleaching owing to the increase in the emission efficiency via plasmon–exciton coupling (Figure S9, Supporting Information).

3. Conclusion

The high-spatiotemporal resolution imaging method with a plasmonic metasurface was applied for monitoring "early molecular events" in the adhesion of 3T3 fibroblasts expressing Venus-paxillin and LifeAct-mScarlet. Fine fibrous nascent adhesions spreading radially at the cell contact position were observed on the SiO_2-coated plasmonic metasurface, temporarily anchoring the cells to the interface while actively moving membrane blebs were maintained during the period before active cell spreading. This fibrous structure is surface-sensitive and was not formed on the fibronectin-preadsorbed cell-adhesive surface. This fibrous nascent adhesion holds a certain morphological similarity to filopodia; however, considering their role, which transiently appears only at the very early stage of cell adhesion and stabilizes the cell contact point by spreading radially, it should be classified as a different protrusion type of cellular structure. This surface-sensitive fibrous structure formed at the nanointerface has potential applications not only in cell adhesion tests of culture substrates but also in single-cell analysis for stimulus response or drug sensitivity and cell discrimination between normal cells and cancer cells in future in combination with a plasmonic metasurface.

4. Experimental Section

Fabrication of the Self-Assembled AuOA Monolayer: Oleylamine-coated gold nanoparticles (AuOAs) were synthesized according to Hiramatsu et al. with some modifications.[47] First, 420 mg (1.0 mmol) of gold(III) chloride acid 4-hydrate was added to a bottle containing a mixture solution composed of 6 mL of oleylamine and 4 mL of toluene and ultrasonicated for 20 min. The mixed solution was transferred to a flask containing 46 mL
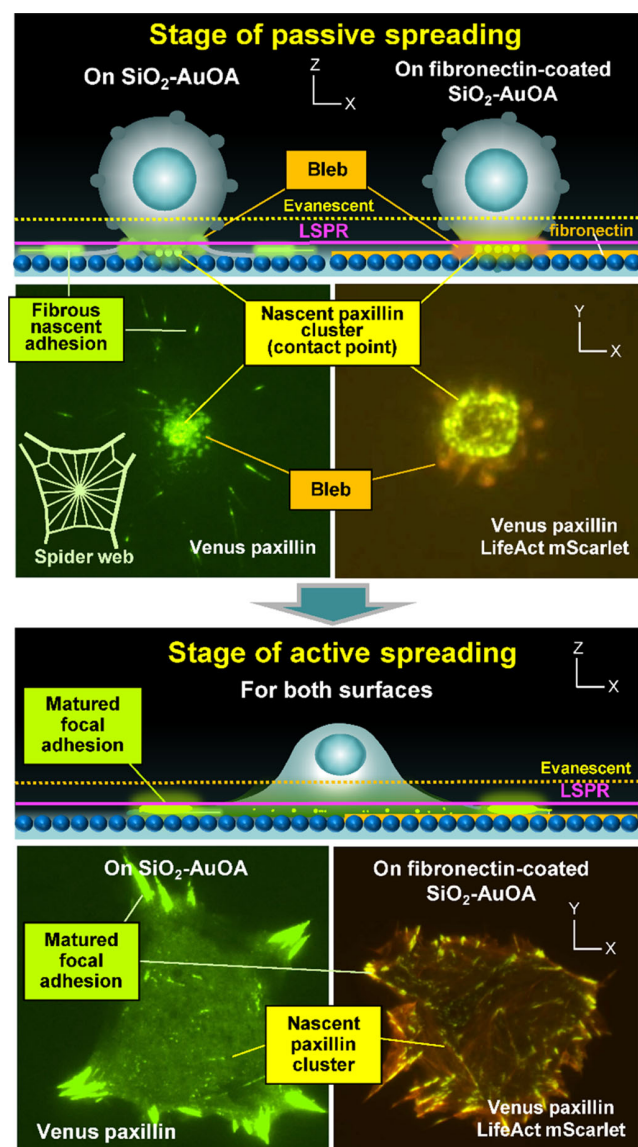
Figure 7. Schematic drawing of the early event of cell spreading on SiO_2 and fibronectin-preadsorbed surfaces.

of toluene and heated and stirred at 125 °C for 60 min in a reflux system. The as-formed AuOAs were heated at 90 °C for another 3 h. Finally, homogenously sized AuOAs with a diameter of 11.8 nm were obtained through three cycles of repeated purification and extraction. The as-synthesized AuOAs were purified by centrifugation at 2000 rpm in toluene-methanol (1:2) mixed solution to remove excess oleylamine. Finally, the extracted AuOAs were redispersed in 3 mL of toluene.

SAMs composed of AuOAs were fabricated in a LB trough (KSV NIMA, Sweden). The hexagonally arranged self-assembled structure of AuOAs in the sheet was characterized by TEM (a JEM-ARM200F instrument, JEOL, Tokyo, Japan) on a TEM grid (U1015: EM Japan) with an acceleration voltage of 200 kV. A 10 or 20 nm-thick SiO_2 layer was deposited on a AuOA sheet by thermal evaporation in a vacuum chamber (R-DEC Co., Ltd., Japan).

Preparation of Biological Samples: 3T3 fibroblasts stably expressing Venus-paxillin were cultured in low-glucose Dulbecco's modified Eagle's medium (DMEM) supplemented with 10% fetal bovine serum (FBS), 100 U mL^{-1} penicillin, 100 μg mL^{-1} streptomycin, and 250 μg mL^{-1} G418.[48,49] The cultured cells were trypsinized when they reached 70% confluency. In total, 9×10^4 cells were seeded onto the AuOA sheet with a 20 nm SiO_2 evaporation layer, which was rinsed twice with sterile phosphate buffered saline (PBS) solution before use. For the experiments with a surface preadsorbed with fibronectin, a 10 nm SiO_2 evaporation layer was mainly utilized, taking into account the thickness of the protein layers. For protein coating, the substrate was incubated with human plasma fibronectin (F2006, Sigma-Aldrich, St. Louis, MO, USA; 10 μg mL^{-1} in PBS) for 30 min and then rinsed with PBS.

The pLifeAct_mScarlet_N1 plasmid was a gift from Dorus Gadella (Addgene plasmid #85 054, Addgene, USA). The plasmid DNA was transformed into *Escherichia coli* DH5 alpha, and plasmid preparation was performed using a Qiagen plasmid mini kit (Qiagen, Tokyo, Japan). For dual-colored observation, 3T3 fibroblasts stably expressing Venus-paxillin were transfected with pLifeAct_mScarlet_N1 using Lipofectamine LTX (Life Technology, Tokyo, Japan) according to the manufacturer's instructions. The transfected cells were seeded onto AuOA sheets, and imaging was performed within 24 h posttransfection.

Live-cell imaging was conducted in a humidified temperature-controlled stage top incubator (TOKAI HIT, Japan) at 37 °C using phenol red-free CO_2-independent Leibovitz's (L-15) medium supplemented with 10% FBS and penicillin/streptomycin.

TIRF Microscopy: Fluorescence time-lapse images of live cells were captured using a commercialized TIRF microscope (ECLIPSE Ti2-E, Nikon, Japan) equipped with a multiple-wavelength laser (LightHUB, Omnicron-Laserage, Laserproducke GmbH, Germany) and a 100× objective lens (CFI Apo TIRF 100 × H/1.49, Nikon, Japan). High-speed dual-color imaging was conducted using a dual-camera image-splitting optical system (W-VIEW GEMINI-2C, Hamamatsu, Japan) with two sets of high-speed CMOS cameras (ORCA-Flash 4.0, Hamamatsu Photonics, Japan). A 514 nm excitation laser and a 542/22 nm bandpass filter were used for Venus-paxillin imaging, while a 561 nm excitation laser and a 615/24 nm bandpass filter were used for LifeAct-mScarlet imaging. The excitation lights were blocked by a shutter when the fluorescence images were not captured in order to avoid photobleaching by continuous illumination. Focus drift during time-lapse imaging was minimized by Perfect Focus System equipped in the microscope. The incidence angle for TIRF imaging was adjusted to 67.5° or 75° beyond the total internal reflection angle. The large incident angle of 75° was employed for dual-color imaging to reduce background fluorescence of LifeAct-mScarlet (derived from molecules in cytosol). The fluorescence image of Venus-paxillin did not change by the incident angle. Image analysis was conducted using NIH ImageJ software.

Supporting Information

Supporting Information is available from the Wiley Online Library or from the author.

[1] M. B. Ginzberg, R. Kafri, M. Kirschner, *Science* **2015**, *348*, 1245075.
[2] J. Malmström, J. Lovmand, S. Kristensen, M. Sundh, M. Duch, D. S. Sutherland, *Nano Lett.* **2011**, *11*, 2264.
[3] Y. Arima, H. Iwata, *J. Mater. Chem.* **2007**, *17*, 4079.
[4] S. R. Ryoo, Y. K. Kim, M. H. Kim, D. H. Min, *ACS Nano* **2010**, *4*, 6587.
[5] C. Von Bilderling, M. Caldarola, M. E. Masip, A. V. Bragas, L. I. Pietrasanta, *Rev. Sci. Instrum.* **2017**, *88*, 013703.
[6] L. MacKay, A. Khadra, *Biophys. J.* **2019**, *117*, 1057.
[7] N. Ibata, E. M. Terentjev, *Biophys. J.* **2020**, *119*, 2063.
[8] M. L. Gardel, I. C. Schneider, Y. Aratyn-Schaus, C. M. Waterman, *Annu. Rev. Cell Dev. Biol.* **2010**, *26*, 315.
[9] D. L. Bodor, W. Pönisch, R. G. Endres, E. K. Paluch, *Dev. Cell* **2020**, *52*, 550.
[10] E. S. Welf, H. E. Johnson, J. M. Haugh, *Mol. Biol. Cell* **2013**, *24*, 3945.
[11] C. Möhl, N. Kirchgeßner, C. Schäfer, K. Küpper, S. Born, G. Diez, W. H. Goldmann, R. Merkel, B. Hoffmann, *Cell Motil. Cytoskeleton* **2009**, *66*, 350.
[12] B. Zimerman, T. Volberg, B. Geiger, *Cell Motil. Cytoskeleton* **2004**, *58*, 143.
[13] R. Zaidel-Bar, C. Ballestrem, Z. Kam, B. Geiger, *J. Cell Sci.* **2003**, *116*, 4605.
[14] K. Jaqaman, J. A. Galbraith, M. W. Davidson, C. G. Galbraith, *Mol. Biol. Cell* **2016**, *27*, 1561.
[15] A. Elosegui-Artola, X. Trepat, P. Roca-Cusachs, *Trends Cell Biol.* **2018**, *28*, 356.
[16] B. Geiger, J. P. Spatz, A. D. Bershadsky, *Nat. Rev. Mol. Cell Biol.* **2009**, *10*, 21.
[17] K. E. Rothenberg, D. W. Scott, N. Christoforou, B. D. Hoffman, *Biophys. J.* **2018**, *114*, 1680.
[18] M. Bergert, T. Lendenmann, M. Zündel, A. E. Ehret, D. Panozzo, P. Richner, D. K. Kim, S. J. P. Kress, D. J. Norris, O. Sorkine-Hornung, E. Mazza, D. Poulikakos, A. Ferrari, *Nat. Commun.* **2016**, *7*, 12814.

**ADVANCED
SCIENCE NEWS**

www.advancedsciencenews.com

**ADVANCED
NANOBIOMED
RESEARCH**
Open Access

www.advnanobiomedres.com

[19] S. Kidoaki, T. Matsuda, *J. Biotechnol.* **2008**, *133*, 225.

[20] M. A. Digman, C. M. Brown, A. R. Horwitz, W. W. Mantulin, E. Gratton, *Biophys. J.* **2008**, *94*, 2819.

[21] M. H. Tong, N. Huang, A. H. W. Ngan, Y. Du, B. P. Chan, *Sci. Rep.* **2017**, *7*, 1.

[22] Y. L. Hu, S. Chien, *Biochem. Biophys. Res. Commun.* **2007**, *357*, 871.

[23] C. K. Choi, J. Zareno, M. A. Digman, E. Gratton, A. R. Horwitz, *Biophys. J.* **2011**, *100*, 583.

[24] M. Vicente-Manzanares, A. R. Horwitz, *J. Cell Sci.* **2011**, *124*, 3923.

[25] J. S. Verdaasdonk, A. D. Stephens, J. Haase, K. Bloom, *J. Cell. Physiol.* **2014**, *229*, 132.

[26] P. Kanchanawong, G. Shtengel, A. M. Pasapera, E. B. Ramko, M. W. Davidson, H. F. Hess, C. M. Waterman, *Nature* **2010**, *468*, 580.

[27] D. C. Worth, M. Parsons, *J. Cell Sci.* **2010**, *123*, 3629.

[28] H. Mazloom-Farsibaf, F. Farzam, M. Fazel, M. J. Wester, M. B. M. Meddens, K. A. Lidke, *PLoS One* **2021**, *16*, e0246138.

[29] T. Azuma, T. Kei, *Opt. Express* **2015**, *23*, 15003.

[30] S. Qin, S. Isbaner, I. Gregor, J. Enderlein, *Nat. Protoc.* **2021**, *16*, 164.

[31] S. L. Gupton, C. M. Waterman-Storer, *Cell* **2006**, *125*, 1361.

[32] S. Masuda, Y. Yanase, Y. E. Usukura, S. Ryuzaki, P. Wang, K. Okamoto, T. Kuboki, S. Kidoaki, K. Tamada, *Sci. Rep.* **2017**, *7*, 1.

[33] S. Masuda, T. Kuboki, S. Kidoaki, S. T. Lee, S. Ryuzaki, K. Okamoto, Y. Arima, K. Tamada, *ACS Appl. Nano Mater.* **2020**, *3*, 11135.

[34] M. Toma, K. Toma, K. Michioka, Y. Ikezoe, D. Obara, K. Okamoto, K. Tamada, *Phys. Chem. Chem. Phys.* **2011**, *13*, 7459.

[35] A. L. Mattheyses, S. M. Simon, J. Z. Rappoport, *J. Cell Sci.* **2010**, *123*, 3621.

[36] E. Usukura, S. Shinohara, K. Okamoto, J. Lim, K. Char, K. Tamada, *Appl. Phys. Lett.* **2014**, *104*, 121906.

[37] A. Ishijima, P. Wang, S. Ryuzaki, K. Okamoto, K. Tamada, *Appl. Phys. Lett.* **2018**, *113*, 171602.

[38] S. Saraswat, A. Desireddy, D. Zheng, L. Guo, H. P. Lu, T. P. Bigioni, D. Isailovic, *J. Phys. Chem. C* **2011**, *115*, 17587.

[39] S. Bhowmick, S. Saini, V. B. Shenoy, B. Bagchi, *J. Chem. Phys.* **2006**, *125*, 181102.

[40] K. Okamoto, D. Tanaka, R. Degawa, X. Li, P. Wang, S. Ryuzaki, K. Tamada, *Sci. Rep.* **2016**, *6*, 1.

[41] D. S. Bindels, L. Haarbosch, L. Van Weeren, M. Postma, K. E. Wiese, M. Mastop, S. Aumonier, G. Gotthard, A. Royant, M. A. Hink, T. W. J. Gadella, *Nat. Methods* **2016**, *14*, 53.

[42] J. T. Wessels, K. Yamauchi, R. M. Hoffman, F. S. Wouters, *Cytom. Part A* **2010**, *77*, 667.

[43] M. Nemethova, S. Auinger, J. V. Small, *J. Cell Biol.* **2008**, *180*, 1233.

[44] S. Munevar, Y. L. Wang, M. Dembo, *Biophys. J.* **2001**, *80*, 1744.

[45] F. Buggenthin, F. Buettner, P. S. Hoppe, M. Endele, M. Kroiss, M. Strasser, M. Schwarzfischer, D. Loeffler, K. D. Kokkaliaris, O. Hilsenbeck, T. Schroeder, F. J. Theis, C. Marr, *Nat. Methods* **2017**, *14*, 403.

[46] M. Doan, A. E. Carpenter, *Nat. Mater.* **2019**, *18*, 414.

[47] H. Hiramatsu, F. E. Osterloh, *Chem. Mater.* **2004**, *16*, 2509.

[48] T. Nagai, K. Ibata, E. Park, M. Kubota, K. Mikoshiba, *Nat. Biotechnol.* **2002**, *20*, 87.

[49] N. Shimada, M. Saito, S. Shukuri, S. Kuroyanagi, T. Kuboki, S. Kidoaki, T. Nagai, A. Maruyama, *ACS Appl. Mater. Interfaces* **2016**, *8*, 31524.